Modeling Saline Mudflat and Aquifer Deformation Synthesizing Environmental and Hydrogeological Factors Using Time-Series InSAR

Wei Xiang ⓘ, Guoxiang Liu ⓘ, Rui Zhang ⓘ, Saeid Pirasteh ⓘ, Xiaowen Wang, Wenfei Mao ⓘ, Song Li, and Lingxiao Xie

Abstract—**Clarifying the surface and subsurface deformation is important for protecting the infrastructures attached to the ground and reasonably exploiting the underground resources. This article presents an improved deformation model combining environmental factors (i.e., precipitation and temperature) with hydrogeological parameters to separate the saline-soil deformation from the aquifer deformation over Qarhan Salt Lake, China. First, the vertical ground deformation was derived by 119 ascending and 113 descending synthetic aperture radar images of Sentinel-1A collected from July 2015 to May 2020. Subsequently, we estimated the deformation components derived from temperature, precipitation, seasonal oscillation, magnitude, and decay coefficient of the hydrodynamic function by the proposed deformation model. The estimated deformation and decay coefficient maps pinpoint the existing and previously unknown faults. Next, we compared our proposed prototype with the sinusoidal and exponentially decaying model to present the reliability and efficiency in separating the deformation components and estimating the decay coefficient. Finally, we collected the stratigraphic data from 50 drilling wells to validate our model results by simulating the cumulative silt and clay layers (aquitard) thickness utilizing the Ordinary Kriging interpolation method. Findings show that by quantifying the aquitard thickness in the drilling wells, there is a strong relationship in the spatial distribution between cumulative thickness and the decay coefficient. The results suggested that both the decay coefficient and the aquitard-layer thickness can be used as the vital parameters to partition hydrogeological units, which provides an opportunity to detect and mitigate the potential geological hazards in the saline mudflat.**

Index Terms—**Dynamic modeling, ground deformation, hydrogeological unit, saline mudflat, time-series InSAR.**

I. INTRODUCTION

S ALT swelling, collapsibility, and corrosion are the major geological properties of saline soil [1], [2]. In particular, the collapsibility of saline soil has the potential for a large deformation after wetting under self-weight or external loads. Since salt crystals can be completely dissolved in water, the internal friction among soil particles decreases rapidly, weakening soil strength [3]. On the contrary, when the temperature rises with intense evaporation or decreases to freezing temperature, salt crystals precipitate, and cement with the soil particles, resulting in salt swelling. Then the internal friction among soil particles increases, strengthening the soil. Because of the salt swelling, the volume of sulfate and chlorine saline soil increases by about 3 and 1.3 times, respectively [4]. Therefore, water penetration and temperature are the major environmental factors that cause the strength changes of saline soil [5]. The external environmental factors are introduced to the correlation analysis in the seasonal deformation of saline soil to make the surface dynamic evolution characteristics more specific and detailed [6]. Moreover, in the modeling of seasonal uplift (frost heave) and subsidence (thaw settlement), precipitation and temperature are mostly used for the deformation modeling in saline-soil and permafrost regions [7].

In addition to the surface deformation of saline soil, the hydraulic head changes in the subsurface aquifer also cause regional deformation [8]. Seasonal meltwater, precipitation, and intense evaporation are the major environmental factors that affect the dynamic changes of the subsurface aquifer system in the saline mudflat. Besides, with the increase of human activities, the extensive exploitation of underground minerals and groundwater exacerbates the abnormal change in the aquifer system. Moreover, the aquifer skeleton deforms with subsurface pore pressure and effective stress changes modulated by water recharge and discharge [9]. Therefore, the groundwater discharge causes the regional settlement at an annual rate of tens of centimeters in the dry seasons [10], while the groundwater recharge makes the ground foundation rebound in the rainy seasons [11]. Hence, the dynamic change of aquifer accompanied by the ground deformation is a common feature in the inland salt lake area [9], [12].

Many potential engineering geological disasters result from the complex deformation caused by hydraulic head changes, salt swelling, and collapsibility [4], [9]. Modeling and interpreting the ground and underground deformation is important for protecting the infrastructures attached to the ground. In the methods for nonlinear deformation modeling, the rectangular hyperbolic
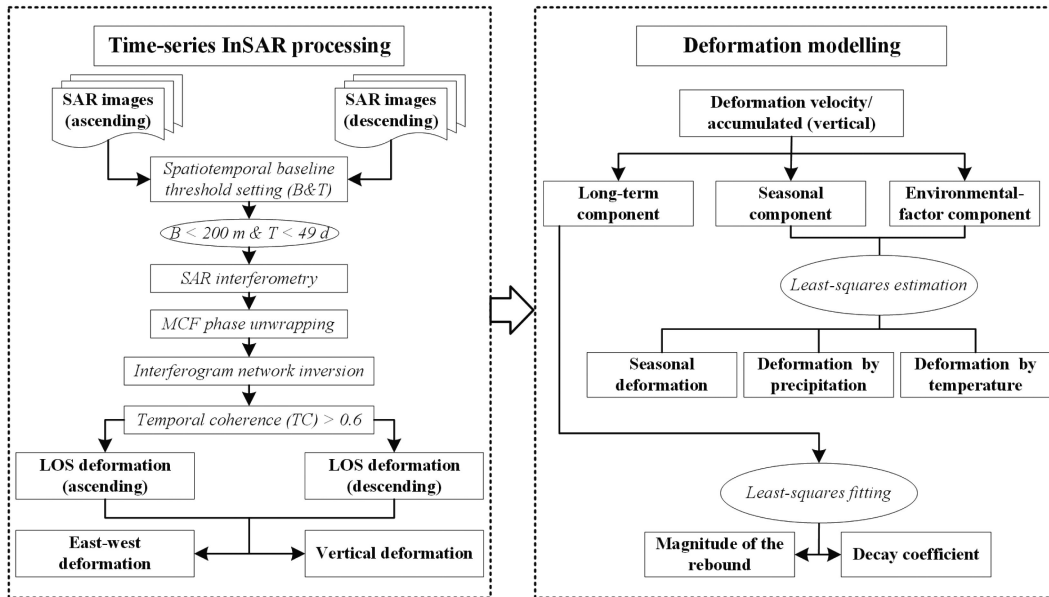
Fig. 1. Time-series InSAR processing and deformation modeling, *B* is the perpendicular baseline, and *T* is the temporal baseline.

model was used for modeling and predicting the settlements of saline-soil formations [13]. The superimposed and sinusoidal model incorporating both deformation styles and temporal components was adopted to simulate the long-term and seasonal permafrost deformation [14]. However, both the hyperbolic and sinusoidal models concentrate on the features of the deformation curve, the influence of the external environmental factor is not taken into account on the deformation. The nonlinear model considering precipitation and temperature factors was applied to separating the deformation components derived from the external environmental factors in the permafrost area [7]. Still, there is no deep underground deformation component in this model. In addition, a superimposed deformation model combining the sinusoidal and the exponentially decaying components was used for presenting the hydrogeological-triggered deformation in Salt Lake City [9]. Although the superimposed deformation model considered the surface deformation and the hydrogeological-triggered deformation in the deep underground, the deformation components derived from the external environmental factors are still confused.

To separate the deformation components caused by the external environmental factors from the deep underground activities and interpret the internal mechanism of such a complex deformation, this article proposed a coupling deformation model combining environmental factors with hydrogeological parameters. First, we adopted the time-series InSAR technique [15]–[18] to extract the surface deformation over Qarhan Salt Lake (QSL) in Qinghai Province of China. Subsequently, the deformation components derived from the aquifer and saline-soil change were separated and accurately estimated by the proposed deformation model. Furthermore, to validate the reliability of the model result and clarify the relationship between the estimated hydrogeological parameters and the geological compositions, we collected the stratigraphic data from 50 drilling wells for statistical analyses. First, the spatial properties of the cumulative aquitard (silt and

clay layers with poor permeability) thickness were simulated by the Ordinary Kriging interpolation method [19], [20]. Then the correlation between the estimated hydrogeological parameters and the cumulative aquitard thickness was quantified by Jaccard similarity coefficients.

II. METHODOLOGY

A. Time-Series InSAR Processing

Due to the daily and monthly fluctuations of the external environmental factors (i.e., temperature and precipitation) in the saline mudflat, it is difficult for saline soil to maintain high coherence for a long time. Therefore, we adopted the time-series InSAR method by constraining the spatiotemporal baseline threshold to obtain the interferograms for good coherences (Fig. 1). In this time-series InSAR method, a network of interferograms is inverted to retrieve surface deformation through time. At last, we set the temporal coherence threshold more than 0.6 to make use of the coherent targets (CTs) with high coherence. We also used the weighted least squares (WLS) estimation to obtain high-precision time-series deformation of the CTs [15], [21], [22]. Fig. 1 shows the time-series InSAR data processing flow chart adopted in this article.

We combined the radar line-of-sight (LOS) deformation of ascending tracks with descending tracks to retrieve the east–west and vertical deformation fields following the approach of [23] and [24]. The sensitivity of LOS deformation to the three-dimensional (3-D) deformation components is different based on the analysis of the imaging geometric parameters of the synthetic aperture radar (SAR) sensor platform. The sensitivity factors of LOS observation to 3-D deformation vectors are expressed as follows [25]:

$$|\partial R/\partial D_e| = |-\cos\varphi\sin\theta| \tag{1}$$

$$|\partial R/\partial D_v| = |-\cos\theta| \tag{2}$$

$$|\partial R/\partial D_n| = |-\sin\varphi\sin\theta|. \tag{3}$$

R is the LOS deformation, D_e, D_n, and D_v are the east–west, the north–south, and the vertical deformations, respectively; φ is the heading angle, and θ is the incidence angle of the satellite. In the QSL area, the heading angles of the satellite paths are $-10.4°$ (ascending) and $-169.6°$ (descending), respectively. The incidence angle is $33.7°$ for ascending tracks and descending tracks. By substituting these parameters into the sensitivity-factor equations, we calculate that the sensitivity factors of Sentinel-1 to east–west, north–south, and vertical displacement are 0.55, 0.10, and 0.83, respectively. Therefore, the observations of InSAR have the highest sensitivity to the vertical deformation, followed by the east–west deformation, and the lowest sensitivity to the north–south deformation. Consequently, the north–south component is poorly resolved, and we thus consider that only the east–west and vertical components of the deformation field are resolved by combining the ascending and descending viewing geometries [11].

B. Deformation Components Considering Hydrodynamic and Environmental Factors

The deformation of the saline mudflat represents the surface dynamic evolution of saline soil and reveals the internal activity of the aquifer system. Since the sedimentary rock salt in the QSL mainly consists of NaCl crystals, high solubility and fast dissolution of the saline soil could cause the ground collapse when increased precipitation or water erosion [26]. On the contrary, the ground uplifts because of salt swelling when the temperature rises with intense evaporation or decreases to freezing temperature [3]. In addition, the pore pressure of the subsurface aquifer system decreases, and the effective vertical stress increases because of the intense evaporation and anthropogenic withdrawal of groundwater. As a result, the decreased pore pressure and the increased stress lead to the occurrence of a centimeter to decimeter regional subsidence [11], [27]. Moreover, the alpine ice–snow meltwater derived from the Kunlun Mountains and the anthropogenic water injection in the salt deposit recharges groundwater. Then the underground pore pressure increases, and effective stress decreases, which causes the regional rebound [28], [29].

Consequently, the deformation is directly related to the precipitation, the temperature, and the hydraulic head changes in the saline mudflat. However, the indoor experiment shows that the silty clay layer with a thickness of 5 mm can prevent water from infiltrating through it for at least one month [30]. The existence and different thickness of the embedded clay lenses with low hydraulic conductivity may result in various time scales of delay for the equilibration to hydraulic head changes [9]. We can perform the delayed response by modeling the long-term vertical deformation as an exponential function of time [8], [11], [31]:

$$d_{\text{long-term}}(t_i; x, r) = M(e^{kt_i} - 1) \tag{4}$$

where $d_{\text{long-term}}$ is the long-term vertical deformation, t_i is the time interval with respect to the reference SAR image, (x, r) represent the azimuth and range coordinate, M is a coefficient that

describes the magnitude of the long-term vertical deformation, and k is the decay coefficient ranges from -1 to 0. We can use the decay coefficient to simulate the decelerated deforming process, and the smaller k is (closer to -1), the faster equilibration is (tends to be stable).

C. Dynamic Modeling of the Saline Mudflat

To characterize the complex deformation mentioned above in the QSL, we need to separate the surface deformation caused by the dynamic evolution of saline soil by the hydraulic head changes. Since the ground surface is underlain by saline soil and generally undergoes both long-term deformation and seasonal undulation, we designed a superimposed model combining long-term deformation, sinusoidal function, and environmental-factor component. Consequently, a novel model of the original time-series deformation (D_{ts}) is constructed by considering hydrodynamic and environmental factors in this article (5):

$$
\begin{aligned}
D_{\text{ts}}(t_i; x, r) \\
= \underbrace{d_{\text{long-term}}(t_i; x, r)}_{\text{long-term component}} \\
+ \underbrace{a_1(x, r) \cdot \sin\left(\frac{2\pi}{T} \cdot t_i\right) + a_2(x, r) \cdot \cos\left(\frac{2\pi}{T} \cdot t_i\right)}_{\text{seasonal component}} \\
+ \underbrace{a_3(x, r) \cdot T(t_i) + a_4(x, r) \cdot P(t_i)}_{\text{environmental-factor component}} + \varepsilon(t_i; x, r) \tag{5}
\end{aligned}
$$

where T is the period of the seasonal undulations (assuming to be one year in this article), a_1, a_2, a_3, and a_4 are the coefficients to be determined, and $\varepsilon(t_i; x, r)$ is the residual errors. The long-term deformation component is often related to the prolonged hydraulic head changes. It is the remainder after subtracting the seasonal component and environmental-factor component from the original time series.

First, we estimate the seasonal and environmental-factor components in (5) with the four unknown parameters: $A = [a_1(x, r), a_2(x, r), a_3(x, r), a_4(x, r)]^{\text{T}}$, and the observational equation is expressed by

$$V = D_{ts} - BA \tag{6}$$

with Eq. (7) shown at the bottom of next page:

The four unknown parameters in (6) are resolved via a least-squares method when the observation times $N \geq 4$, by assuming that the observations are with equal weights:

$$A = (B^T B)^{-1} B^T D_{ts}. \tag{8}$$

Last, the two unknown parameters (M and k) of the remainder long-term deformation component in (5) are resolved by the least-squares curve-fitting method.

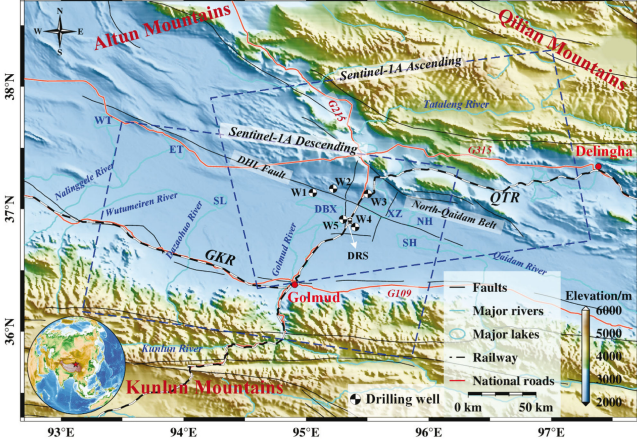| Name	Latitude (°N)	Longitude (°E)	Excavation time	Excavation depth (m)	Groundwater level (m)	Altitude (m)
W1	37.09	95.07	Oct. 2, 2002	14.02	0.48	2679.99
W2	37.14	95.13	Mar. 31, 1966	24.46	8.85	2683.58
W3	37.11	95.50	May. 15, 1986	250.23	/	2780.21
W4	36.91	95.37	Oct. 22, 2002	17.42	2.15	2679.37
W5	36.93	95.34	Sep. 15, 1982	17.50	0.60	2678.69

Fig. 2. Major salt lakes on the map, including the WT (West Taijinar), ET (East Taijinar), SL (Suli), DBX (Dabuxun), XZ (Xiezuo), NH (North Huobuxun), and SH (South Huobuxun); two important railway corridors including the QTR (Qinghai–Tibet Railway) and GKR (Golmud–Korla Railway).

III. Study Area and Data Source

A. Geological Settings

The QSL (36.6267°~37.2097°N, 94.2528°~96.2431°E) is the largest playa in the eastern Qaidam Basin, which is surrounded by Altun Mountains, Qilian Mountains, and Kunlun Mountains [32]. The Dabuxun–Huobuxun Lake (DHL) fault is along the northern margin of the Qarhan playa and divides the area into two distinct geological units (Fig. 2). Large nonmarine evaporite deposits in the southern part of the DHL fault are formed during the Pliocene–Quaternary [33]. These nonmarine evaporite deposits mainly consist of salt and siliciclastic sediments, and their thicknesses range from 40 to 70 m [34].

To understand the geological compositions of the QSL thoroughly, we plotted the sedimentary structure of the Holocene salt layer by five sample drilling wells (Table I). The locations and stratigraphic sections of them are shown in Figs. 2 and 3.

These drilling wells are both located in the northern part (W2 and W3) and southern part (W1, W4, and W5) of the DHL fault (Fig. 2). From the stratigraphic sections (Fig. 3), we can know that the major geological compositions are sand and clay in the northern part. Thus this subregion is usually called sand flat. The major geological composition is rock salt in the southern part and is usually called saline mudflat. Many silty clay layers with thicknesses ranging from centimeters to meters are found in the sedimentary formation of rock salt.

B. Hydrogeological Settings

The QSL consists of 10 shallow perennial and ephemeral salt lakes, including West Taijinar, East Taijinar, Suli, Dabuxun, Tuanjie, Xiezuo, South Huobuxun, and North Huobuxun [32]. The area of the QSL is 5,856 km², with a length of 168 km from east to west and a width of 20–40 km from north to south. The QSL has an inland plateau desert climate with an average annual precipitation of 24 mm and a potential evaporation capacity of 3,564 mm [35]. Because of the dry and rainless climatic circumstances, most salt lakes have become dry and saline mudflats. Dabuxun Salt Lake is the largest salt lake in the Qarhan playa and deposits the potash salt carnallite ($MgCl_2 \cdot KCl \cdot 6H_2O$) along its shores [36]. The rivers that originated from the Kunlun Mountains are Wutumeiren River, Golmud River, Nuomuhong River, and Qaidam River. These mentioned rivers are the major inflows to the QSL. The Golmud River, with a discharge of 7.98×10^8 m³/year, flows northward from the eastern Kunlun Mountains into Dabuxun [35]. In addition, spring waters that discharge along the DHL fault are also the main water replenishment of the Dabuxun Salt Lake [36]. It is worth mentioning that the river flow is controlled by the seasonal meltwater from the surrounding mountains with more abundant water in summer and less in winter [37].

$$B = \begin{bmatrix} \sin\left(\dfrac{2\pi}{T} \cdot (t_2 - t_1)\right) & \cos\left(\dfrac{2\pi}{T} \cdot (t_2 - t_1)\right) & T(t_2) - T(t_1) & P(t_2) - P(t_1) \\ \sin\left(\dfrac{2\pi}{T} \cdot (t_3 - t_1)\right) & \cos\left(\dfrac{2\pi}{T} \cdot (t_3 - t_1)\right) & T(t_3) - T(t_1) & P(t_3) - P(t_1) \\ \sin\left(\dfrac{2\pi}{T} \cdot (t_4 - t_1)\right) & \cos\left(\dfrac{2\pi}{T} \cdot (t_4 - t_1)\right) & T(t_4) - T(t_1) & P(t_4) - P(t_1) \\ \cdots & \cdots & \cdots & \cdots \\ \sin\left(\dfrac{2\pi}{T} \cdot (t_{N+1} - t_1)\right) & \cos\left(\dfrac{2\pi}{T} \cdot (t_{N+1} - t_1)\right) & T(t_{N+1}) - T(t_1) & P(t_{N+1}) - P(t_1) \end{bmatrix}_{N \times 4} . \quad (7)$$
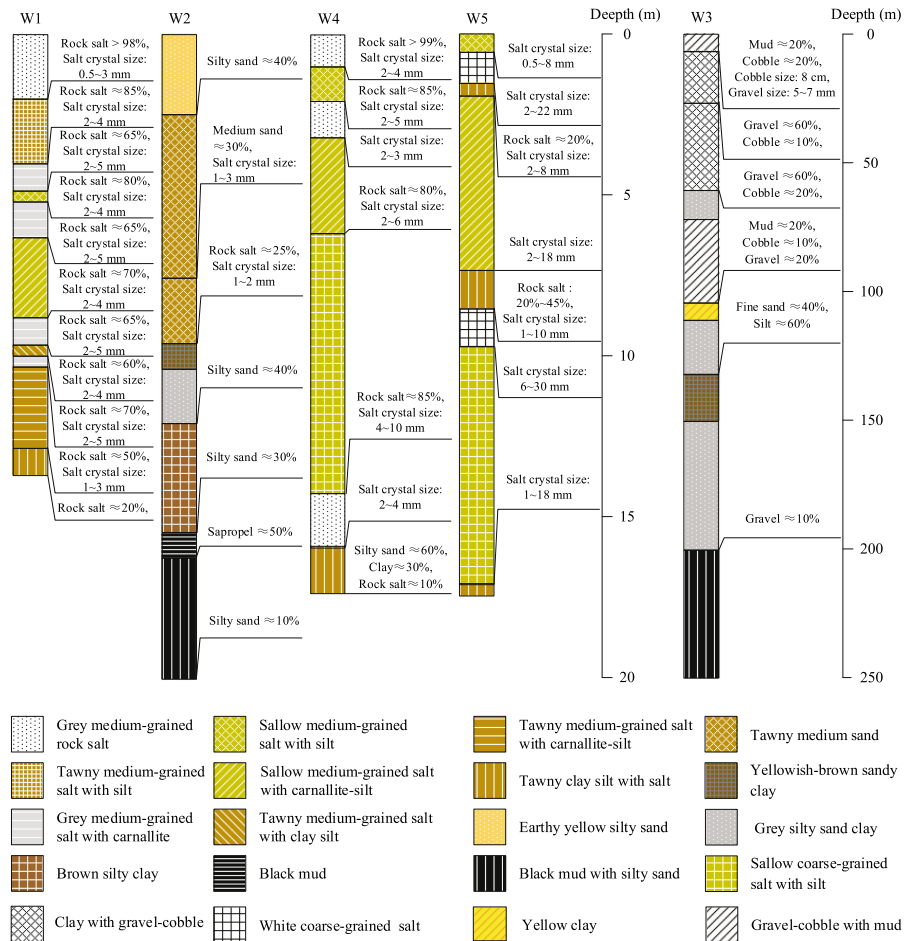
Fig. 3. Stratigraphic sections of drilling wells provided by the China Geological Survey (CGS).[1]

C. Human Activities

Human activities influence the aquifer stability of the QSL because it is the largest soluble potassium and magnesium salt deposit in China; it contains abundant natural solid and liquid resources, i.e., potassium, sodium, magnesium, boron, lithium, and bromide. The total resources of the various salts are more than 6×10^{10} tons [38], among which the reserves of KCl are 5.4×10^8 tons, accounting for 97% of the proven reserves in China. The reserves of $MgCl_2$ are 16.5×10^8 tons, LiCl 8×10^6 tons, and NaCl 4.262×10^{10} tons, which all take first place in China. The annual production capacity of KCl was 0.5 million tons in 1996, 1.05 million tons in 2006, and had exceeded 5 million tons in 2015[2]. Artificial exploitation reduces the amount of high-concentration brine. As a result, the confined water intrudes and dissolves the rock salt of the underground soil layer. Then many subsurface salt caves by water erosion come out and result in the collapse of the ground [26]. In addition, the hydraulic head changes caused by the water discharge and recharge in the underground aquifer could lead to the subsidence

TABLE II
SAR DATASETS INFORMATION

Satellite	Time-span	Image No.	Azimuth angle (°)	Off-nadir angle (°)	Interferograms
Sentinel-1A	201507-202005	119	-10.41 (Ascending)	33.71	391
Sentinel-1A	201507-202005	113	-169.62 (Descending)	33.74	347

and rebound of the ground. Consequently, artificial mining activities accelerate engineering geological disasters such as ground collapse, building destruction, and road damage [39].

D. InSAR Data

The surface deformation of the QSL is derived by 119 ascending and 113 descending SAR images of Sentinel-1A. The spatial resolution of the SAR images (C-band with a wavelength of ~5.6 cm) is 2.33 m $\times$ 13.97 m (range $\times$ azimuth), and the temporal resolution is usually 12 days. We used the VV-polarized SAR images collected from July 2015 to May 2020 to extract the radar LOS deformation for ascending and descending tracks, respectively (Table II). The topographic phase contribution was
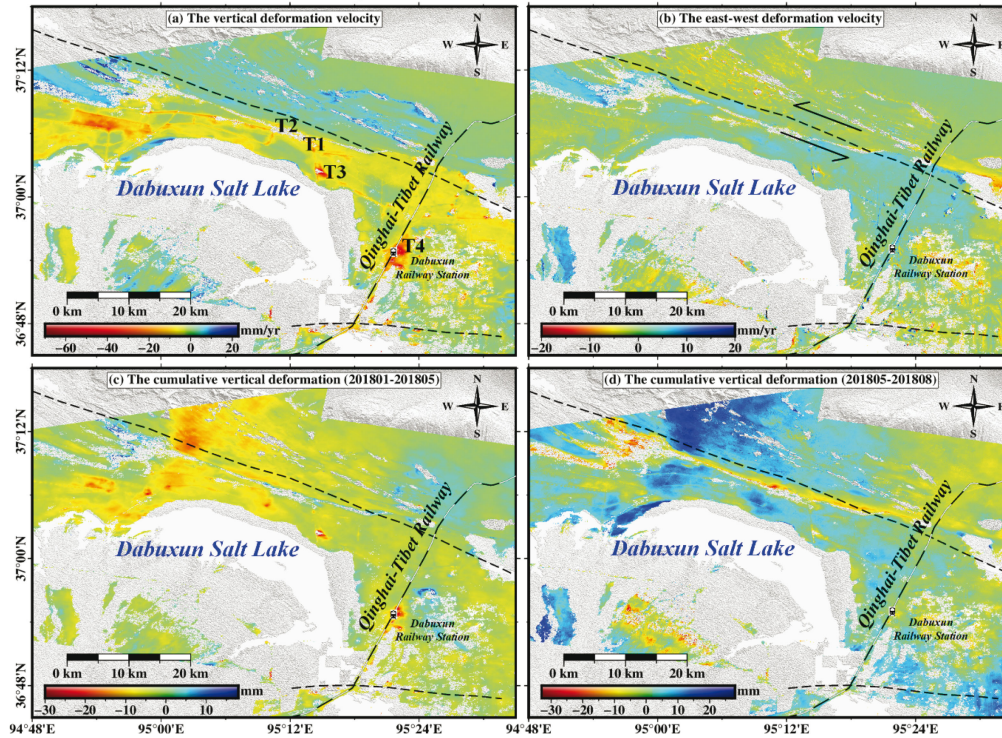
Fig. 4.   Deformation velocity and seasonal deformation in the QSL, the black dotted lines indicate the faults provided by the China Earthquake Administration. (a) Vertical deformation velocity between July 2015 and May 2020 and indicating subsidence in red. (b) East–west deformation velocity between July 2015 and May 2020 and indicating eastward movement in blue. (c) Seasonal deformation in the winter months between January 2018 and May 2018. (d) Seasonal deformation in the summer months between May 2018 and August 2018.

removed by a digital elevation model with a resolution of 30 m generated through the shuttle radar topography mission. Besides, the orbital and the atmospheric delay errors were removed by the precise orbit data provided by the European Space Agency[3] and the GACOS data [40], respectively.

IV. EXPERIMENTS AND RESULTS

We adopted the time-series InSAR method by constraining a temporal baseline threshold within 49 days and a perpendicular baseline within 120 m to obtain the interferograms. As a result, 391 interferograms for ascending tracks and 347 interferograms for descending tracks are selected to estimate the deformation, respectively. Then we proposed a deformation model to characterize the dynamic evolution of the study area synthesizing stratigraphic data, environmental factors (i.e., temperature and precipitation), and hydrogeological parameters (i.e., magnitude and decay coefficient of the hydrodynamic function).

A. Deformation Field of the Study Area

The vertical deformation velocity map between July 2015 and May 2020 indicates an obvious deformation differentiation between the northern and southern parts of the DHL fault [Fig. 4(a)]. The subsidence is between 0–70 mm/year in the southern part of the DHL fault, while uplift is between

0–20 mm/year in the north. The significant and localized subsiding sites (up to 70 mm/year from 2015 to 2020) affected by human activities are the Dabuxun Railway Station and the underground brine mining areas around the Dabuxun Salt Lake. We suspect that such a special phenomenon is because the DHL fault separates the region into two distinct geological units. The east–west deformation velocity map shows that there is also an opposite deformation trend between the two sides of the DHL fault [Fig. 4(b)]. Eastward movement occurs in the southern part of the DHL fault and westward movement in the northern part. The different movement directions along the fault indicate that the DHL fault is a left-lateral strike-slip fault, coinciding with the fault demarcation of the China Earthquake Administration.

B. Time-Series Vertical Deformation of the Typical Feature Points

The deformation velocity map helps us to understand the spatial features of the deformation field. Nevertheless, the deformation velocity map could not figure out the time-series deformation, especially the seasonal dynamics of saline soil and aquifer system. To present the time-series deformation characteristics with high temporal resolution (less than 15 days) in the study area, we selected four typical feature CTs [Fig. 4(a) and Table III] and plotted their cumulative deformations [Fig. 5(a) and (b)]. Two feature CTs in the northern part of the DBX Salt Lake can reflect the deformation features of saline soil and the DHL fault. Another two CTs are located in the brine-exploitation
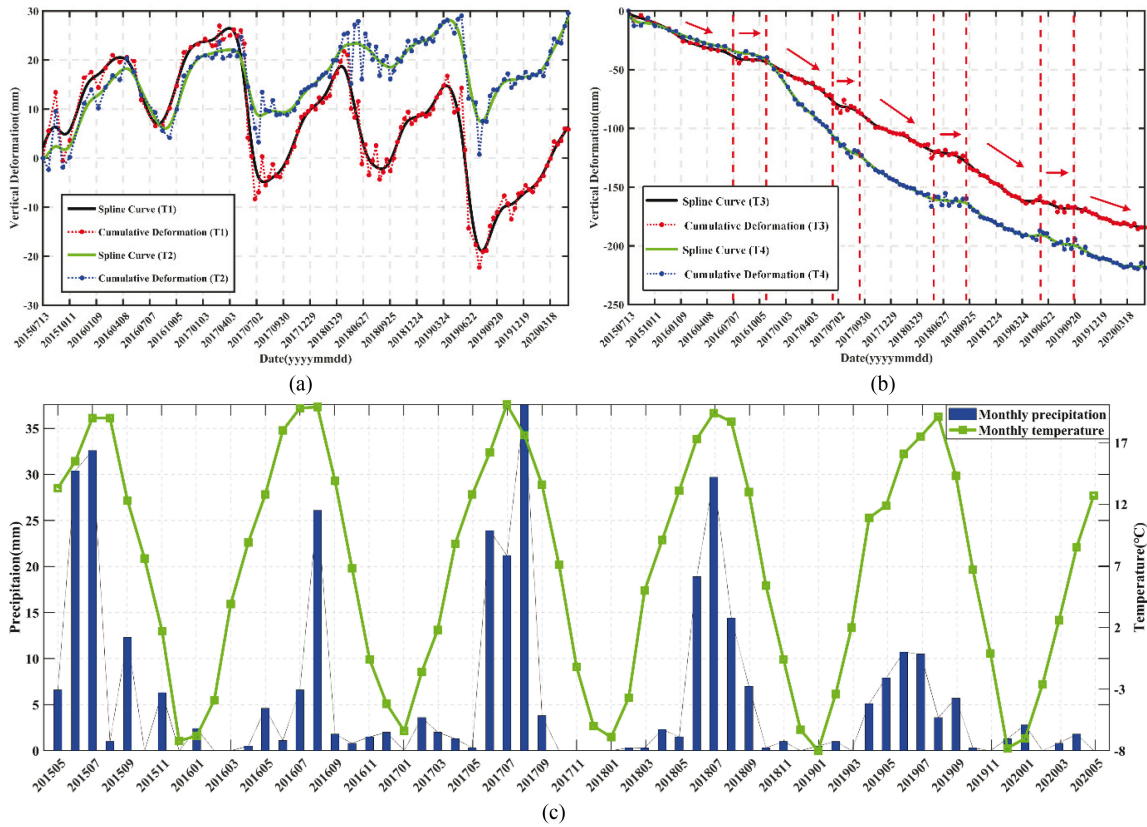
Fig. 5. Time-series vertical deformation of points T1–T4 and the monthly precipitation and temperature. (a) Cumulative deformations of T1 and T2, in red and blue, respectively. (b) Cumulative deformations of T3 and T4, in red and blue, respectively. (c) Monthly precipitation and temperature of Golmud Station (36.417°N, 94.9°E, https://www.ncdc.noaa.gov/cdo-web/datasets/GHCND/stations/GHCND:CHM00052818/detail) from May 2015 to May 2020, in the blue histogram and green line, respectively.

TABLE III
LATITUDE AND LONGITUDE COORDINATES OF THE FOUR FEATURE POINTS

Points' number	Latitude (°N)	Longitude (°E)	Points' number	Latitude (°N)	Longitude (°E)
T1	37.0935	95.2379	T3	37.0368	95.2524
T2	37.1082	95.2029	T4	36.9129	95.3726

area and Dabuxun Railway Station, which are directly influenced by human activities.

Points T1 and T2 are located in the northern and southern parts of the DHL fault, respectively. Obvious seasonal oscillation is the representative feature of their time-series deformation. We suspect that the sharp subsidence after May is mainly caused by the salt collapsibility in rainy seasons from May to August [Fig. 5(a) and (c)]. However, after July [Fig. 5(a) and (c)], a rapid uplift is probably caused by the salt swelling and groundwater recharge in the dry seasons. The dynamic creep of the compression-shear thrust fault (the DHL fault) brings out the uplift trend of point T1 and the subsidence trend of point T2. Points T3 and T4 [Fig. 5(b)] reveal the deformation features of the brine-exploitation area and Dabuxun Railway Station, and either of them has a general subsidence trend that the cumulative deformation is ~200 mm from 2015 to 2020. Although the brine

exploitation is going on, the subsidence trend breaks off during July through September. The findings show that the subsidence due to brine extraction is almost equal to the uplift because the water recharge by the precipitation and the meltwater from the surrounding mountains.

To sum up, both in the saline-soil area of the natural environment and the area affected by human activity, the ground deformation is directly connected with aquifer and saline-soil dynamics. Seasonal precipitation and temperature are the main factors that cause the seasonal deformation of saline soil on the surface. The groundwater discharge resulted from the brine exploitation, and strong evaporation makes the localized foundation sink. Nevertheless, the groundwater recharge by the meltwater from the glacier and precipitation causes the rebound of the foundation. That is why we separated the deformation components caused by the dynamics of surface saline soil and the subsurface aquifer system and analyzed their influences on the dynamic evolution of the study area.

C. Estimated Coefficients for the Improved Deformation Model

To separate the deformation components caused by the dynamics of surface saline soil and the subsurface aquifer system, a superimposed model combining long-term deformation, sinusoidal function, and environmental-factor component is adopted
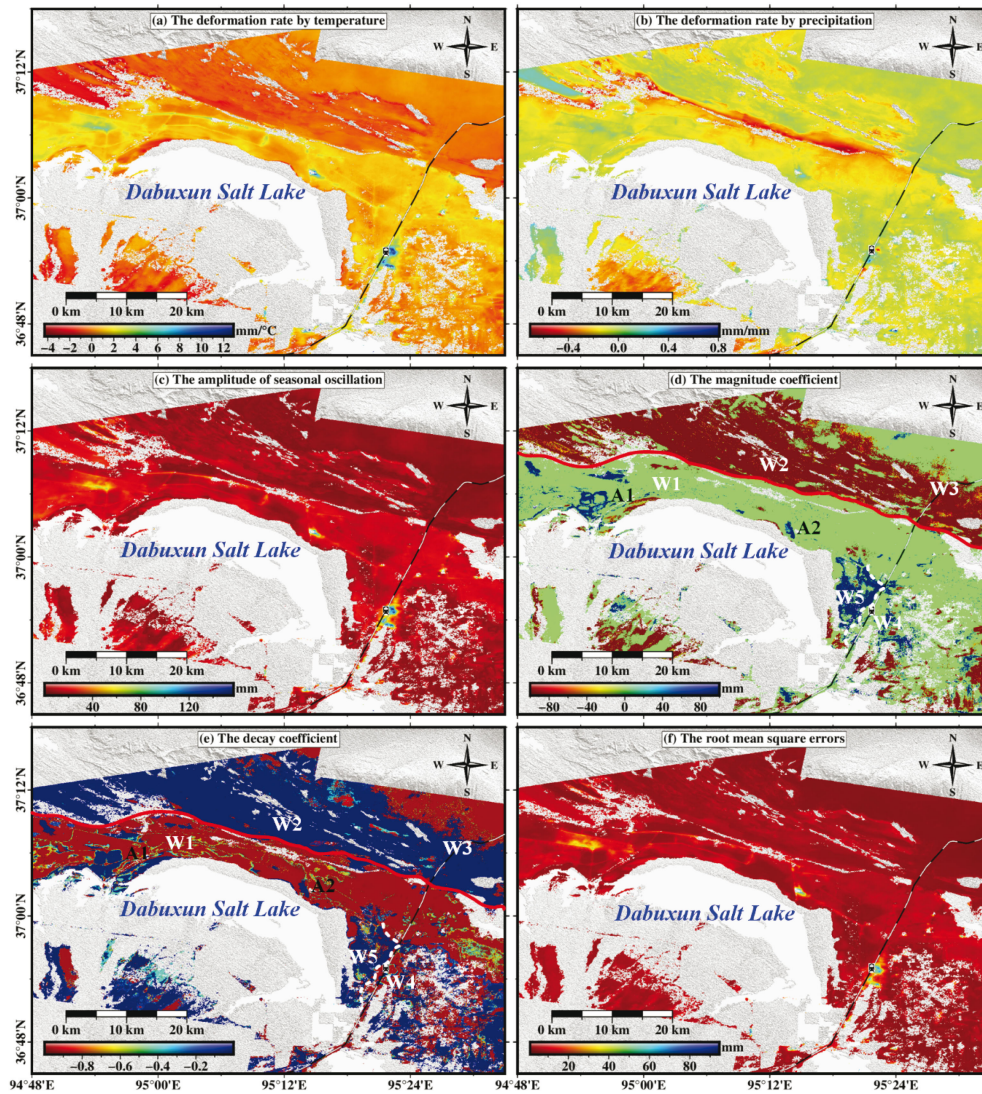
Fig. 6. Estimated coefficients for the improved deformation model, including saline-soil deformation and exponentially decaying deformation. (a) Estimated coefficients accounting for air temperature ($a3$). (b) Estimated coefficients accounting for precipitation ($a4$). (c) Amplitude of seasonal oscillations (m). (d) Magnitude coefficient (M), the red line indicates the DHL fault, and the white dash line indicates the previously unknown fault. (e) Decay coefficient (k). (f) RMSE of the exponentially decaying model.

in this article. The estimated coefficients in (4) and (5) describe the different components of the ground deformation. On the overall trend, the deformation in the saline mudflat is proportional to temperature [Fig. 6(a)] and inversely proportional to precipitation [Fig. 6(b)]. However, the ground deformation is proportional to precipitation in the brine-exploitation areas. Therefore, we suspect that this abnormal phenomenon is because of the groundwater recharge by the increased precipitation. The deformation rate caused by temperature ranges from −4 to 13 mm/°C, and precipitation ranges from −0.7 to 0.8 mm/mm. The amplitude of seasonal oscillations (i.e., $m = \sqrt{a_1(x,r)^2 + a_2(x,r)^2}$) ranges from 0 to 150 mm [Fig. 6(c)] and is larger in the saline mudflat than in the sand flat. The amplitudes in the brine-exploitation areas and the Dabuxun Railway Station are generally very large due to the surface disturbance associated with artificial exploitation, engineering construction, and carriage operation [14].

We can preliminarily classify the environmental-factor components (the deformations caused by temperature and precipitation) to the dynamic evolution of saline soil. The seasonal oscillations are influenced by both the saline-soil deformation and the hydrologically driven deformation. After that, the long-term decay coefficient describes the long-term delayed ground response to hydraulic head changes, which is estimated by the least-squares curve-fitting of (4). The distributions of fault systems on the maps of decay coefficient [Fig. 6(d) and (e)] and deformation velocity [Fig. 4(a) and (b)] reveal that the faults partition the hydrogeological units and control the deformation field [9]. Furthermore, the decay coefficients show a noticeable difference on the two sides of the DHL fault. Therefore, we can determine the position of the DHL fault more accurately by using the maps of decay coefficient [red lines in Fig. 6(d) and (e)]. In particular, we identified another previously unknown fault located in the west of Dabuxun Railway Station from the decay
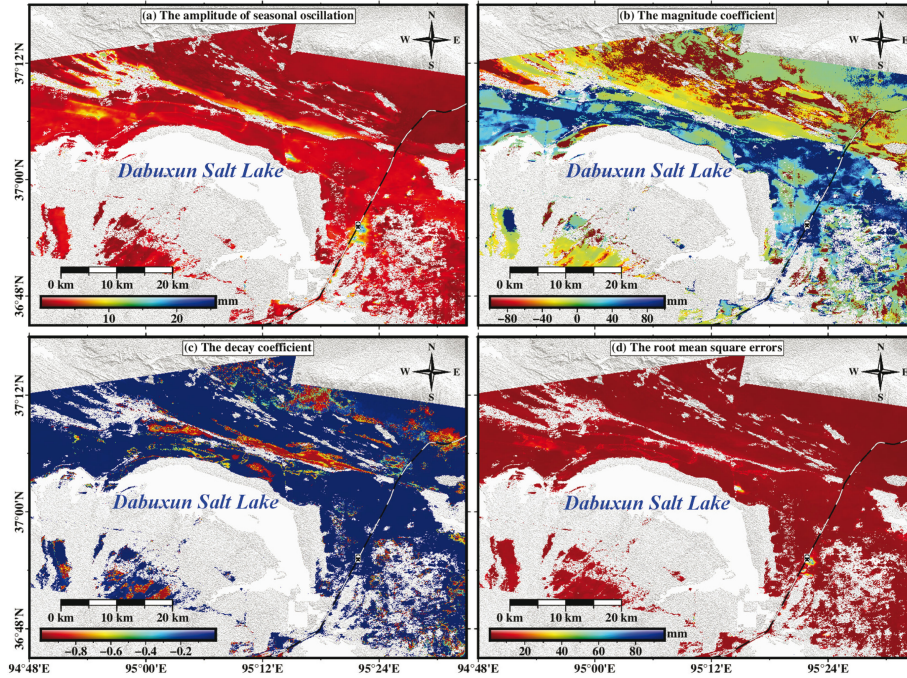
Fig. 7.   Estimated coefficients for the sinusoidal and the exponentially decaying model.
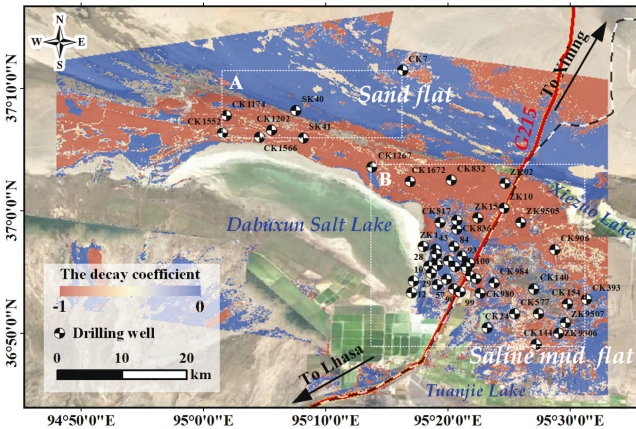

Fig. 8.   Distribution of 50 drilling wells in areas A and B, the base map is the decay coefficient and satellite image.

TABLE IV
CUMULATIVE THICKNESS OF AQUITARD IN AREA A

No.	Name	Latitude (°N)	Longitude (°E)	Altitude (m)	depth (m)	thickness (m)
1	CK7	37.1916	95.2716	2680.09	7.52	7.52
2	SK40	37.1371	95.1263	2683.57	12.1	4
3	SK41	37.0991	95.1363	2678.63	11.98	0
4	CK1566	37.1002	95.0764	2679.99	14.02	0
5	CK1552	37.1061	95.0263	2677.95	22.1	0.3
6	CK1174	37.1300	95.0319	2678.19	7.87	0.65

head change. Similarly, the decay coefficients are mostly closer to 0 in the northern part of the DHL fault, which means slower equilibration. In particular, the decay coefficients of brine-exploitation areas around the Dabuxun Salt Lake are closer to 0 [see areas A1 and A2 in Fig. 6(d) or (e)], which is different from other areas in the saline mudflat. The root-mean-square errors in areas A1 and A2 are also greater than in other areas. We suspect that this is due to the accelerated or quasi-linear deformation trend [Fig. 5(b)] in the areas with anthropogenic activities.

V. DISCUSSION

A. Subregion Division and Stratigraphic Structure Characteristics

We can know from the deformation velocity maps [Fig. 4(a) and (b)] that the stability of the ground foundation is different on the two sides of the DHL fault. The ground foundation is more stable in the northern part of the DHL fault. To better understand this special deformation field, we collected the geological data and plotted the stratigraphic structures of five sample drilling wells in the QSL region (wells W1–W5 in Figs. 2 and 3). The

coefficient map [see white dashed lines in Fig. 6(d) and (e)]. The previously unknown fault is about 38.5 km long and almost 25.7 km of it runs along the railway. Moreover, the short-est distance between the fault and the railway is about 237 m.

The values of magnitude coefficient [Fig. 6(d)] are mostly positive in the saline mudflat around the Dabuxun Salt Lake, which means net subsidence in the chronological deformation from 2015 to 2020 [Fig. 4(a)]. However, the magnitude coeffi-cients are negative, indicating net uplift in the northern part of the DHL fault, which is consistent with the deformation velocity map [Fig. 4(a)]. The decay coefficients are mostly closer to −1 in the saline mudflat around the Dabuxun Salt Lake, suggesting that the ground deformation is faster equilibrated to the hydraulic
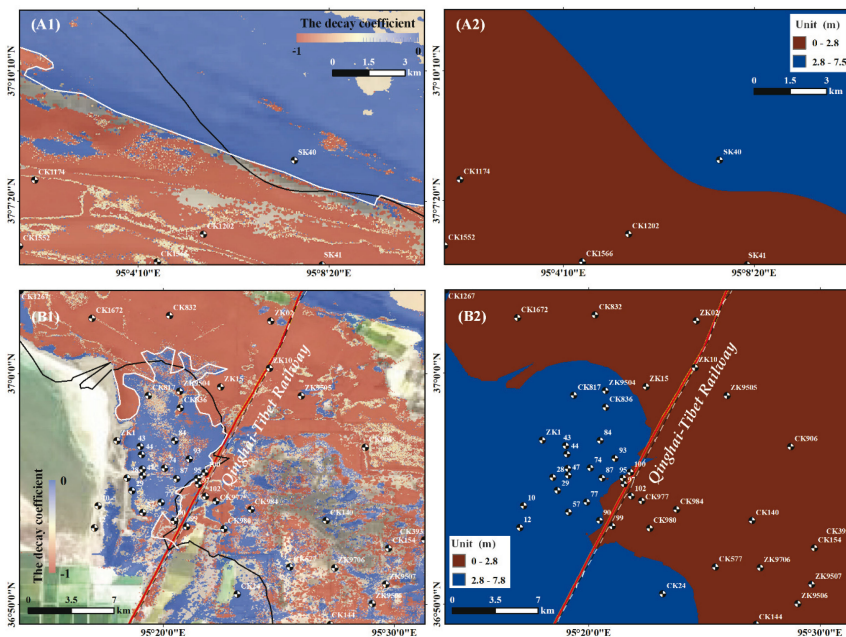
Fig. 9. (A1) and (B1) are the decay coefficient map in areas A and B, respectively. (A2) and (B2) are the cumulative thickness of aquitard simulation maps by the Ordinary Kriging interpolation method in areas A and B, respectively. The white lines in (A1) and (B1) are the clear boundaries between the coefficient of 0 and −1, and the black lines are the boundaries with a cumulative thickness of 2.8 m in (A2) and (B2).
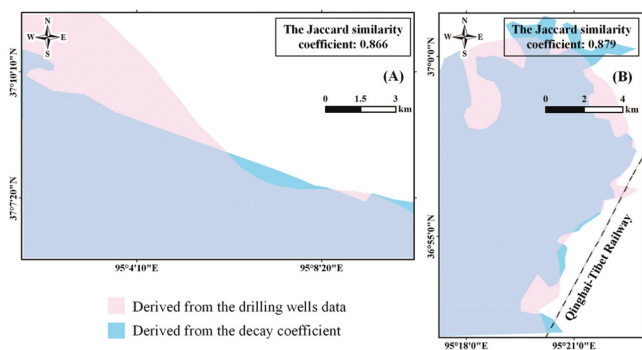

Fig. 10. Jaccard similarity coefficients of the selected subregions derived from the drilling wells data and the decay coefficient in areas A and B.

basic properties of these five drilling wells are stated in Table I. Wells (i.e., W2 and W3) are located in the northern part of the DHL fault, and the material compositions of their stratigraphic structures are mostly sand and clay between 2663 and 2683 m above sea level (Fig. 3 and Table I). On the other hand, Wells (i.e., W1, W4, and W5) are close to the QSL in the southern part of the DHL fault, and the major material composition of their stratigraphic structures is rock salt (Fig. 3).

Consequently, we can divide the study area into two distinct subregions (sand flat and saline mudflat) using the DHL fault as the demarcation line. The deformation velocity of the sand flat in the northern part of the DHL fault is close to 0 mm/year, which suggests that the ground foundation of the sand flat is relatively stable. However, the ground foundation of the saline mudflat is weak in the southern part of the DHL fault, with significant subsidence velocity from 2015 to 2020.

Although the spatial features of the deformation field show a similar subsidence trend in the saline mudflat [Fig. 4(a)], we cannot understand whether there are subregions with different hydrogeological characteristics only by the deformation velocity map. However, the decay coefficient can reveal the ground response to the hydraulic head changes and be a reference index for the division of hydrogeological units [9]. From the estimated coefficients for the improved deformation model, we realized that some subregions with different hydrogeological characteristics [see the areas around W4 and W5 in Fig. 6(d) and (e)] exist in the saline mudflat. To demonstrate the reasonability of the hydrogeological units' division by the decay coefficient, we collected the stratigraphic data of areas around W4 and W5 and then compared their stratigraphic distribution (see wells W1, W4, and W5 in Fig. 3). The altitudes of wells W1, W4, and W5 are roughly equal to 2679 m, and their major composition is rock salt. However, there are two silty clay layers with low hydraulic conductivity (in the depth of 1.5–1.85 m and 7.6–8.6 m, respectively) in the stratigraphic structure of well W5, and they can prevent water from infiltrating through them for a long time [30]. The comparison result proves that the thicker the silty clay layer, the closer the decay coefficient is to 0 and the longer the ground response to the hydraulic head change is.

B. Comparison of the Proposed Prototype With the Sinusoidal and Exponentially Decaying Model

The proposed deformation model in this article considered the saline-soil deformation and took the precipitation and temperature data into the estimation model. To present the superiority of the proposed model in separating the deformation components and estimating the decay coefficient, we compared the estimated

coefficients of the proposed deformation model in this article with the sinusoidal and exponentially decaying model. Therefore, we removed the precipitation and temperature components in (5), and the sinusoidal and exponentially decaying model is expressed by

$$
\begin{aligned}
D_{\mathrm{ts}}&(t_i; x, r) \\
&= \underbrace{d_{\mathrm{long-term}}(t_i; x, r)}_{\mathrm{long-term\ component}} \\
&+ \underbrace{a_1(x, r) \cdot \sin\left(\frac{2\pi}{T} \cdot t_i\right) + a_2(x, r) \cdot \cos\left(\frac{2\pi}{T} \cdot t_i\right)}_{\mathrm{seasonal\ component}} \\
&+ \varepsilon(t_i; x, r).
\end{aligned}
\tag{9}
$$

As we know from the deformation maps and the existing faults in the QSL area, the DHL fault divides the study area into two subregions (i.e., sand flat and saline mudflat). However, there is no demarcation line along the DHL fault in the estimated decay coefficient map derived from the sinusoidal and exponentially decaying model [Fig. 7(c)]. As a result, most decay coefficients representing the hydrodynamic activities in the sand flat and the saline mudflat are the same and close to 0, which is inconsistent with the hydrogeological unit division in this region. The reason is that the temperature and precipitation directly influence the saline-soil deformation. Thus, we need to separate the surface deformation caused by the saline-soil evolution and estimate the decay coefficient accurately.

C. Hydrodynamic Characteristics Validated by Stratigraphic Data

We can roughly know from Sections A and B that the decay coefficient has a certain relationship with the silty clay layers in the stratigraphic structure because the thickness of the silty clay layer affects the permeability of the groundwater and directly relates to the surface deformation. Therefore, finding out the relationship between the thickness of the silty clay layer and the decay coefficient is very important for understanding the safety of the underground structure and the constructions attached to the saline soil in the study area. Nevertheless, how the silty clay layer affects the decay coefficient's magnitude is challenging to quantify only by those five drilling wells data. Thus, we collected the stratigraphic data from 50 drilling wells in the study area and performed statistical analysis on these data.

The statistical analysis and the Ordinary Kriging interpolation result showed that the spherical semivariogram model best fits the thickness of clay and soil. The internal relationship between the decay coefficient and silty clay can be sought from the angle of quantization. The 50 drilling wells are distributed in two typical areas (A and B) and are good representatives of different subregions derived from the decay coefficient map (Fig. 8). There are 6 and 44 drilling wells for simulating the cumulative thickness distribution in areas A and B, respectively.

However, because the silty clay layer with low hydraulic conductivity in the stratigraphic structure can prevent water from infiltrating through them, their cumulative thickness is the key

TABLE V
CUMULATIVE THICKNESS OF AQUITARD IN AREA B

No.	Name	Latitude (°N)	Longitude (°E)	Altitude (m)	depth (m)	thickness (m)
1	77	36.9072	95.3319	2678.7	16.5	3.17
2	74	36.9318	95.3345	2678.7	24	4.43
3	45	36.9313	95.3183	2678.8	17.5	2.68
4	10	36.9046	95.2865	2678.3	20	9.28
5	57	36.8999	95.3188	2678.8	16	1.87
6	12	36.8888	95.2838	2678.4	16	10.64
7	28	36.9249	95.3075	2678.8	17	1.93
8	47	36.9265	95.3187	2678.8	17	3.1
9	87	36.9244	95.3429	2678.6	23	1.69
10	93	36.9386	95.3523	2678.6	17.5	4.96
11	29	36.9156	95.3109	2678.8	16.5	4.3
12	CK836	36.9754	95.3456	2678.8	20.95	7.65
13	97	36.9203	95.3588	2678.7	17.5	1.9
14	90	36.8939	95.3412	2678.8	17	5.5
15	99	36.8898	95.3502	2678.7	18	1.96
16	102	36.9116	95.364	2678.9	23.2	0.81
17	CK977	36.9081	95.3716	/	22.66	0
18	CK980	36.8882	95.3773	/	21.17	0.2
19	100	36.9288	95.3635	2678.9	22.5	2.89
20	95	36.9246	95.3581	2678.8	17.5	3.83
21	CK984	36.902	95.3967	/	20.94	0.1
22	CK577	36.8605	95.4246	2678.5	20.3	1.55
23	CK24	36.841	95.3867	2678.9	15.45	6.65
24	CK817	36.9843	95.3227	2678.8	23.09	4.27
25	ZK9504	36.9874	95.3454	2678.7	13.97	4.86
26	ZK1	36.9517	95.3	2679.0	187.7	2.8
27	43	36.9476	95.3168	2678.7	24.08	5.87
28	44	36.9417	95.3178	2678.6	22.52	3.9
29	84	36.9516	95.3416	2678.7	24	3.27
30	ZK15	36.9905	95.3747	2679.1	37.05	0
31	CK906	36.947	95.479	2679.6	29.5	0
32	ZK9505	36.984	95.433	2679.6	39.6	0
33	ZK02	37.038	95.411	2679.0	29.5	0
34	ZK10	37.004	95.41	2678.5	23.4	0
35	CK832	37.042	95.338	2678.5	17.45	0
36	CK1672	37.04	95.282	2678.9	16.44	1.04
37	CK1267	37.06	95.23	2678.9	12.4	3.55
38	ZK9706	36.86	95.457	2679.7	16.44	0
39	ZK9507	36.848	95.494	2677.1	23.35	0
40	ZK9506	36.834	95.484	2676.5	27.43	0
41	CK140	36.894	95.451	2679.0	17.51	1.9
42	CK393	36.88	95.522	2679.1	20.52	0.85
43	CK154	36.874	95.496	2678.9	18.6	0.16
44	CK144	36.819	95.454	2679.2	16.27	1.55

factor affecting the response between hydraulic head change and surface deformation. The rock salt, especially coarse-grained salt has strong water permeability in the saline mudflat; the strata with silt and clay elements in the drilling wells are classified as aquitard in our statistics. The cumulative thicknesses of aquitard in the 50 drilling wells are calculated in Tables IV and V, respectively. All of these 50 drilling wells data are provided by CGS.[4] As the depths of the drilling wells are different, we chose the shallowest depth as the common depth for statistics. Therefore, we only count the stratigraphic data at a mutual depth of 7.52 m in area A and 16 m in area B, respectively.

Furthermore, the cumulative thickness statistical analysis of this article showed that the boundaries with a cumulative thickness of 2.8 m in both areas A and B are very close to the boundaries of the decay coefficient (Fig. 9). Since there is no drilling well data in the northwest part of area A, a deviation

[4][Online]. Available: http://zk.cgsi.cn/

between the boundary of simulated results and the boundary of the decay coefficient map has been seen. However, the boundary with a cumulative thickness of 2.8 m near SK40 [Fig. 9(A2)] shows good agreement with the boundary of the decay coefficient map [Fig. 9(A1)] in the northern part of the DHL fault. A total of 44 drilling wells are distributed in area B (Figs. 8 and 9), especially denser around Dabuxun Railway Station. Therefore, the simulated result derived from the Ordinary Kriging interpolation method shows more detailed boundary information and good consistent with the boundary of the decay coefficient map [Fig. 9(B1) and (B2)].

For quantifying the correlation between the two results that derived from the decay coefficient and the drilling wells data, we calculated the Jaccard similarity coefficients (i.e., ($S_{decay} \cap S_{well}$)/($S_{decay} \cup S_{well}$), where S_{decay} is the subregion derived from the drilling wells data, and S_{well} is the subregion derived from the drilling wells data in areas A and B, respectively (Fig. 10). The Jaccard similarity coefficient is 0.866 in area A and 0.879 in area B, suggesting that our estimated decay coefficient is consistent with the result derived from the drilling wells data. As we have described in part IV, the decay coefficient is used to determine the existing fault's position and identify the previously unknown fault. Furthermore, the cumulative thickness of the aquitard affects the hydraulic conductivity and has a strong spatial correlation with the decay coefficient. Consequently, in addition to the estimated decay coefficient, we suggest that the cumulative thickness of aquitard in 2.8 m can be used as a reference thickness to separate the two different subregions in the QSL.

VI. Conclusion

This article contributed a designed coupling deformation model combining environmental parameters with hydrodynamic factors. Such a creative deformation model can separate the deformation components derived from saline soil and hydraulic head change. Moreover, the seasonal deformation induced by the precipitation, temperature, seasonal oscillations, and aquifer are modeled and accurately estimated. Therefore, the improved high-precision deformation components provide a data guarantee for the subsequent hydrodynamic analysis. Furthermore, by modeling and calculating the decay coefficient, the position of the existing DHL fault is accurately determined. Moreover, a new fault has been found from the decay coefficient map in the western part of the Dabuxun Railway Station.

To support and validate the reliability of the estimated decay coefficient, which is an essential basis for the classification of different hydrogeological units and the determination of fault location, we collected stratigraphic data from 50 drilling wells, and then conducted a statistical analysis and Ordinary Kriging interpolation. The statistical analysis concluded that the cumulative thickness of silt and clay layers that affect the water permeability in the stratigraphic structure could be used as a vital parameter to simulate the surface response to the hydraulic head change. Therefore, we counted the silt and clay layers with poor permeability as the aquitard. Moreover, we simulated their cumulative thickness in the stratigraphic structure by using the

Ordinary Kriging interpolation method. The simulation results showed that the isoline of 2.8 m in the cumulative aquitard thickness is in a good agreement with the boundary of a mutated change from 0 to −1 in the decay coefficient. Consequently, the aquitard with a cumulative thickness of 2.8 m in our study area is used as a reference thickness to distinguish the rapid and immediate surface deformation from the long-term and slow surface deformation caused by the hydraulic head change. Finally, we concluded that the proposed model and research results help detect potential geological hazards in the construction and operation phases of large-scale infrastructure (especially the railway crossing different geological units) in such a complex geological environment.

References

[1] D. Y. Wang, J. K. Liu, and X. Li, "Numerical simulation of coupled water and salt transfer in soil and a case study of the expansion of subgrade composed by saline soil," *Procedia Eng.*, vol. 143, pp. 315–322, Dec. 2016.

[2] Y. M. Lai, D. Y. Wu, and M. Y. Zhang, "Crystallization deformation of a saline soil during freezing and thawing processes," *Appl. Thermal Eng.*, vol. 120, pp. 463–473, 2017.

[3] C. L. Wang, C. X. Jiang, Q. Xie, and T. Feng, "Change in microstructure of salty soil during crystallization," *J. Southwest Jiaotong Univ.*, vol. 1, pp. 69–72, Feb. 2007.

[4] W. X. Bao, "Study on engineering properties and engineering classification of inland saline soil," Ph.D. dissertation, Chang'an Univ., Xi'an, China, 2009.

[5] Y. Zhang, J. H. Fang, J. K. Liu, and A. H. Xu, "Experimental research on physical properties of saline soil subgrade filler in Chaerhan region," *Sci. Cold Arid Regions*, vol. 7, no. 3, pp. 0212–0215, Jul. 2015.

[6] W. Xiang et al., "Saline-soil deformation extraction based on an improved time-series InSAR approach," *ISPRS Int. J. Geo-Inf.*, vol. 10, no. 3, Feb. 2021, Art. no. 112.

[7] R. Zhao, Z. W. Li, G. C. Feng, Q. J. Wang, and J. Hu, "Monitoring surface deformation over permafrost with an improved SBAS-InSAR algorithm: With emphasis on climatic factors modeling," *Remote Sens. Environ.*, vol. 184C, pp. 276−287, Jul. 2016.

[8] M. M. Miller, M. Shirzaei, and D. Argus, "Aquifer mechanical properties and decelerated compaction in Tucson, Arizona," *J. Geophys. Res., Solid Earth*, vol. 122, pp. 8402–8416, Oct. 2017.

[9] X. Hu, Z. Lu, and T. Wang, "Characterization of hydrogeological properties in Salt Lake Valley, Utah, using InSAR," *J. Geophys. Res.: Earth Surf.*, vol. 123, no. 6, pp. 1257–1271, May 2018.

[10] J. W. Bell, F. Amelung, A. R. Ramelli, and G. Blewitt, "Land subsidence in Las Vegas, Nevada, 1935–2000: New geodetic data show evolution, revised spatial patterns and reduced rates," *Environ. Eng. Geosci.*, vol. 8, no. 3, pp. 155–174, Mar. 2002.

[11] E. Chaussard, S. Wdowinski, E. Cabral-Cano, and F. Amelung, "Land subsidence in central Mexico detected by ALOS InSAR time-series," *Remote Sens. Environ.*, vol. 140, pp. 94–106, Jan. 2014.

[12] E. Chaussard, R. Bürgmann, M. Shirzaei, E. J. Fielding, and B. Baker, "Predictability of hydraulic head changes and characterization of aquifer-system and fault properties from insar-derived ground deformation," *J. Geophys. Res., Solid Earth*, vol. 119, no. 8, pp. 6572–6590, Jul. 2015.

[13] M. A. Al-Shamrani, "Applicability of the rectangular hyperbolic method to settlement predictions of Sabkha soils," *Geotech. Geol. Eng.*, vol. 22, no. 4, pp. 563−587, Dec. 2004.

[14] Z. W. Li *et al.*, "InSAR analysis of surface deformation over permafrost to estimate active layer thickness based on one-dimensional heat transfer model of soils," *Sci. Rep.*, vol. 5, Oct. 2015, Art. no. 15542.

[15] Y. J. Zhang, H. Fattahi, and F. Amelung, "Small baseline InSAR time series analysis: Unwrapping error correction and noise reduction," *Comput. Geosci.*, vol. 133, Sep. 2019, Art. no. 104331.

[16] A. Mehrabi *et al.*, "Observing new evidence of intensified activity of the anar fault based on the persistent scatterer interferometry and radon anomaly," *Remote Sens.*, vol. 13, May 2021, Art. no. 2072.

[17] Z. J. Zhang, M. M. Wang, X. G. Liu, C. Wang, and H. Zhang, "Map and quantify the ground deformation around salt lake in Hoh Xil, Qinghai-Tibet Plateau using time-series InSAR from 2006 to 2018," *IEEE J. Sel. Topics Appl. Earth Observ. Remote Sens.*, vol. 14, pp. 858–869, Oct. 2020, Art. no. 20266468.

[18] L. J. Zhu, X. M. Xing, Y. K. Zhu, W. Peng, Z. H. Yuan, and Q. Xia, "An advanced time-series InSAR approach based on poisson curve for soft clay highway deformation monitoring," *IEEE J. Sel. Topics Appl. Earth Observ. Remote Sens.*, vol. 14, pp. 7682–7698, Jul. 2021, Art. no. 21052789.

[19] A. A. Daya, "Reserve estimation of central part of Choghart north anomaly iron ore deposit through ordinary Kriging method," *Int. J. Mining Sci. Technol.*, vol. 22, no. 4, pp. 573–577, Jul. 2012.

[20] K. Hasan., S. Paul, T. J. Chy, and A. Antipova, "Analysis of groundwater table variability and trend using ordinary Kriging: The case study of Sylhet, Bangladesh," *Appl. Water Sci.*, vol. 11, no. 7, Jun. 2021, Art. no. 120.

[21] A. Ferretti, A. Fumagalli, F. Novali, C. Prati, F. Rocca, and A. Rucci, "A new algorithm for processing interferometric data-stacks: SqueeSAR," *IEEE Trans. Geosci. Remote Sens.*, vol. 49, no. 9, pp. 3460–3470, May 2011.

[22] H. Ansari, F. D. Zan, and R. Bamler, "Efficient phase estimation for interferogram stacks," *IEEE Trans. Geosci. Remote Sens.*, vol. 56, no. 7, pp. 4109−4125, May 2018.

[23] X. W. Wang *et al.*, "3D coseismic deformations and source parameters of the 2010 Yushu earthquake (China) inferred from DInSAR and multiple-aperture InSAR measurements," *Remote Sens. Environ.*, vol. 152, pp. 174−189, Jul. 2014.

[24] X. W. Wang, G. X. Liu, B. Yu, K. R. Dai, and Z. L. Li, "An integrated method based on DInSAR, MAI and displacement gradient tensor for mapping the 3D coseismic deformation field related to the 2011 Tarlay Earthquake (Myanmar)," *Remote Sens. Environ.*, vol. 170, pp. 388−404, Oct. 2015.

[25] X. J. Zha, R. S. Fu, and Z. Y. Dai, "The sensitivity of DInSAR to surface deformation in different direction," *Acta Geodaetica et Cartographica Sinica*, vol. 35, no. 2, pp. 133−137, May 2006.

[26] B. L. Gao, J. C. Wang, and Y. Li, "Research on the salt soluble disasters of saline lake subgrade along the Qinghai-Tibet railway in Chaerhan Salt Lake region," *J. Railway Eng. Soc.*, vol. 32, no. 5, pp. 6–11, May 2015.

[27] J. W. Bell, F. Amelung, A. Ferretti, M. Bianchi, and F. Novali, "Permanent scatterer InSAR reveals seasonal and long-term aquifer-system response to groundwater pumping and artificial recharge," *Water Resour. Res.*, vol. 44, Feb. 2008, Art. no. W02407.

[28] F. Amelung, D. L. Galloway, J. W. Bell, H. A. Zebker, and R. J. Laczniak, "Sensing the ups and downs of Las Vegas: InSAR reveals structural control of land subsidence and aquifer-system deformation," *Geology*, vol. 27, no. 6, pp. 483−486, Jun. 1999.

[29] Z. Lu and W. R. Danskin, "InSAR analysis of natural recharge to define structure of a groundwater basin, San Bernardino, California," *Geophys. Res. Lett.*, vol. 28, no. 13, pp. 2661–2664, Jul. 2001.

[30] Y. T. Jiang, "Genesis of clastic intercalation in salt-bearing strata of Qarhan Salt Lake in Qaidam Basin," master's dissertation, China Univ. Geosci., Beijing, China, 2019.

[31] M. M. Miller and M. Shirzaei, "Spatiotemporal characterization of land subsidence and uplift in phoenix using InSAR time series and wavelet transforms," *J. Geophys. Res., Solid Earth*, vol. 120, pp. 5822–5842, Jul. 2015.

[32] H. C. Wei *et al.*, "Chemical elements in core sediments of the qarhan salt lake and palaeoclimate evolution during 94–9 ka," *Acta Geoscientica Sinica*, vol. 37, no. 2, pp. 193–203, Apr. 2016.

[33] Q. S. Fan *et al.*, "Sr Isotope and major ion compositional evidence for formation of Qarhan Salt Lake, Western China," *Chem. Geol.*, vol. 497, pp. 128–145, Sep. 2018.

[34] R. Q. Li, C. L. Liu, P. C. Jiao, W. P. Liu, and S. J. Wang, "The present situation, existing problems, and countermeasures for exploitation and utilization of low-grade potash minerals in Qarhan Salt Lake, Qinghai Province, China," *Carbonates Evaporites*, vol. 35, Mar. 2020, Art. no. 34.

[35] S. S. Yu, H. B. Tan, X. Q. Liu, and G. Cao, *Sustainable Utilization of Qarhan Salt Lake Resources*. Beijing, China: Science Press, 2009, pp. 3−39.

[36] T. K. Lowenstein, R. J. Spencer, and P. X. Zhang, "Origin of ancient potash evaporites: Clues from the modem nonmarine Qaidam basin of western China," *Science*, vol. 245, no. 4922, pp. 1090–1092, Sep. 1989.

[37] Z. C. Zhang and S. Z. Wang, "Long-term monitoring of subgrade stability of the Qinghai-Tibet railway in the Charhan Playa region," in. *Proc. Int. Symp. Eng. Complex Rock Formations*, 1988, pp. 915−921.

[38] S. J. Wang, "Prospects for tapping the resources of the Qarhan Salt lake," *Geol. Chem. Minerals*, vol. 21, no. 3, pp. 175–180, 1999.

[39] G. Modeste, C. Doubre, and F. Masson, "Time evolution of mining-related residual subsidence monitored over a 24-year period using InSAR in Southern Alsace, France," *Int. J. Appl. Earth Observ. Geoinf.*, vol. 102, Jun. 2021, Art. no. 102392.

[40] C. Yu, Z. H. Li, and N. T. Penna, "Interferometric synthetic aperture radar atmospheric correction using a GPS-based iterative tropospheric decomposition model," *Remote Sens. Environ.*, vol. 204, pp. 109–121, Jan. 2018.
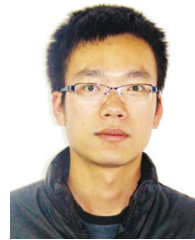
Wei Xiang received the B.Eng. and M.Eng. degrees in surveying engineering from the China University of Geosciences, Wuhan, China, in 2012 and 2014, respectively. Since 2017, he has been working toward the Ph.D. degree in photogrammetry and remote sensing with the Faculty of Geosciences and Environmental Engineering, Southwest Jiaotong University, Chengdu, China.

His research interests include geological hazard monitoring and time-series InSAR.

Guoxiang Liu received the B.Eng. degree in surveying engineering from the East China Institute of Geology, Jiangxi, China, in 1991, the M.Eng. degree in geomatics from the Southwest Jiaotong University, Chengdu, China, in 1994, and the Ph.D. degree in remote sensing from The Hong Hong Ploytechnic University, Hong Kong, in 2003.

He is currently a Professor with the Department of Remote Sensing and Geospatial Information Engineering, Southwest Jiaotong University. From September 2005 to September 2006, he was a Visiting Scholar and conducted research on InSAR with Dr. S. M. Buckley with the Department of Aerospace Engineering and Engineering Mechanics, The University of Texas, Austin, TX, USA. He has authored three books, more than 170 articles, and holds 12 patents. His research interests include InSAR, PSI, radargrammetry, and digital photogrammetry for mapping regional topography, and deformation.

Prof. Liu was a Cochair of the Working Group VII of the ISPRS Technical Commission VII, and a member of the Commission on Mapping from Satellite Imagery of the International Cartographic Association.

Rui Zhang received the B.Eng. degree in mechanical engineering from the North China University of Water Resources and Electric Power, Henan, China, in 2004, and the M.Eng. degree in geographic information engineering and the Ph.D. degree in remote sensing from the Southwest Jiaotong University, Chengdu, China, in 2008 and 2012, respectively.

He is currently an Associate Professor with the Faculty of Geosciences and Environmental Engineering, Southwest Jiaotong University. From 2012 to 2014, he was a Postdoctoral Fellow with The Institute of Space and Earth Information Science, The Chinese University of Hong Kong, Hong Kong. His research interest includes the development of ground deformation monitoring and early warning system, fundamental study of microware remote sensing, and synthetic aperture radar interferometry.

Prof. Zhang was a recipient of the Best Paper Award of the 2nd International Workshop on Earth Observation and Remote Sensing Application in 2012, and the Annual Excellent Paper Award of the Journal of Remote Sensing in 2019.

Saeid Pirasteh received the Ph.D. degree in geology (remote sensing and GIS) from Aligarh Muslim University, Aligarh, India, in 2004, and the Ph.D. degree in geography (GIS, geoanalytics, and LiDAR) from the University of Waterloo, Waterloo, ON, Canada, in 2018.

He is currently an Associate Professor with the Faculty of Geosciences and Environmental Engineering, Southwest Jiaotong University, Chengdu, China. His research interests include remote sensing and LiDAR data processing and geology applications, environmental hazards, and disaster assessment toward implementing UN sustainable development goals 2030. He is also interested in integrating artificial intelligence, machine learning, computer vision, development of geospatial algorithms, models, software, mobile, and web app in geosciences applications.

Dr. Pirasteh is the UN-GGIM Academic Network Member.

Xiaowen Wang received the B.S. degree in geomatics from Henan Polytechnic University, Jiaozuo, China, in 2006, and the Ph.D. degree in photogrammetry and remote sensing from Southwest Jiaotong University, Chengdu, China, in 2017.

He is currently an Associate Professor with the Faculty of Geosciences and Environmental Engineering, Southwest Jiaotong University, Chengdu, China, where he is mainly involved in crustal deformation measuring and modeling using remote sensing techniques, such as Interferometric Synthetic Aperture Radar, optical image cross-correlation, and digital elevation model differencing.

Wenfei Mao received the B.Eng. and M.Eng. degrees in surveying engineering from the East China University of Technology, Fuzhou, China, in 2013 and 2018, respectively. Since 2018, he has been working toward the Ph.D. degree in photogrammetry and remote sensing with the Faculty of Geosciences and Environmental Engineering, Southwest Jiaotong University, Chengdu, China.

His research interests include ionospheric modeling and correcting for InSAR/TS-InSAR based on GNSS and SAR, and geological hazard monitoring.

Song Li received the B.S. degree in the surveying engineering from Shandong University of Science and Technology, Qingdao, China, in 2020. He is currently working toward the M.S. degree in photogrammetry and remote sensing with the Faculty of Geosciences and Environmental Engineering, Southwest Jiaotong University, Chengdu, China.

His research interests include fire remote sensing.

Lingxiao Xie received the B.S. degree in surveying engineering from the School of Geography, Geomatics and Planning, Jiangsu Normal University, Jiangsu, China, in 2019. He is currently working toward the M.S. degree in photogrammetry and remote sensing with the Faculty of Geosciences and Environmental Engineering, Southwest Jiaotong University, Chengdu, China.

His research interests include research in remote sensing and risk assessment of forest fires.